Multi-terminal transport measurements of MoS$_2$ using a van der Waals heterostructure device platform

Xu Cui[1†], Gwan-Hyoung Lee[2*†], Young Duck Kim[1†], Ghidewon Arefe[1], Pinshane Y. Huang[3], Chul-Ho Lee[4], Daniel A. Chenet[1], Xian Zhang[1], Lei Wang[1], Fan Ye[5], Filippo Pizzocchero[6], Bjarke S. Jessen[6], Kenji Watanabe[7], Takashi Taniguchi[7], David A. Muller[3,8], Tony Low[9], Philip Kim[10] and James Hone[1*]

Atomically thin two-dimensional semiconductors such as MoS$_2$ hold great promise for electrical, optical and mechanical devices and display novel physical phenomena. However, the electron mobility of mono- and few-layer MoS$_2$ has so far been substantially below theoretically predicted limits, which has hampered efforts to observe its intrinsic quantum transport behaviours. Potential sources of disorder and scattering include defects such as sulphur vacancies in the MoS$_2$ itself as well as extrinsic sources such as charged impurities and remote optical phonons from oxide dielectrics. To reduce extrinsic scattering, we have developed here a van der Waals heterostructure device platform where MoS$_2$ layers are fully encapsulated within hexagonal boron nitride and electrically contacted in a multi-terminal geometry using gate-tunable graphene electrodes. Magneto-transport measurements show dramatic improvements in performance, including a record-high Hall mobility reaching 34,000 cm^2 V^{-1} s^{-1} for six-layer MoS$_2$ at low temperature, confirming that low-temperature performance in previous studies was limited by extrinsic interfacial impurities rather than bulk defects in the MoS$_2$. We also observed Shubnikov–de Haas oscillations in high-mobility monolayer and few-layer MoS$_2$. Modelling of potential scattering sources and quantum lifetime analysis indicate that a combination of short-range and long-range interfacial scattering limits the low-temperature mobility of MoS$_2$.

Following the many advances in basic science and applications of graphene, other two-dimensional materials, especially the transition-metal dichalcogenides (TMDCs), have attracted significant interest for their fascinating electrical, optical and mechanical properties[1–8]. Among the TMDCs, semiconducting MoS$_2$ has been the most widely studied. It has a thickness-dependent electronic band structure[3,5], reasonably high carrier mobility[1,2,6–9] and demonstrates novel phenomena such as coupled spin–valley physics and the valley Hall effect[10–14], leading to various applications including transistors[1,7,15], memories[16], logic circuits[17,18], light-emitters[19] and photodetectors[20] with flexibility and transparency[2,21]. However, as with any two-dimensional material, the electrical and optical properties of MoS$_2$ are strongly affected by impurities and its dielectric environment[1,2,9,22], hindering the study of its intrinsic physics and limiting the design of devices based on such two-dimensional materials. In particular, the theoretical upper bound of the electron mobility of monolayer (1L) MoS$_2$ is predicted to range from several tens to a few thousands at room temperature and exceed 10^5 cm^2 V^{-1} s^{-1} at low temperature (T) depending on the dielectric environment, impurity density and charge carrier density[23–25]. In contrast, experimentally measured 1L MoS$_2$ devices on SiO$_2$ substrates have exhibited a room-temperature two-terminal field-effect mobility ranging from 0.1 to 55 cm^2 V^{-1} s^{-1}

(refs 1,26,27). This value increases to 15–60 cm^2 V^{-1} s^{-1} with encapsulation by high-k dielectric materials[1,9] due to a more effective screening of charged impurities[24]. Owing to the presence of large contact resistance from the metal–MoS$_2$ Schottky barrier, however, these two-terminal measurements underestimate the true channel mobility[7,28,29]. Multi-terminal Hall mobility measurements[8,9] still show a mobility substantially below theoretical limits, particularly at low T, with best reported values of 174 cm^2 V^{-1} s^{-1} at 4 K for 1L (ref. 9) and 250 cm^2 V^{-1} s^{-1} and 375 cm^2 V^{-1} s^{-1} at 5 K for 1L and 2L devices, respectively (ref. 8). Typically, these thin samples exhibit a crossover to non-metallic behaviour at carrier densities below ~1×10^{13} cm^{-2} (refs 8,9,30) or at smaller carrier densities by the engineering of local defect states and improved interfacial quality[31]. The scattering and disorder that lead to this non-metallic behaviour can arise from multiple origins, such as lattice defects, charged impurities in the substrates and surface adsorbates, and it has been difficult to identify their separate contributions[1,8,9,23,30–33].

van der Waals device with tunable graphene contact

We have previously demonstrated that the encapsulation of graphene within hexagonal boron nitride (hBN) reduces scattering from substrate phonons and charged impurities, resulting in band

[1]Department of Mechanical Engineering, Columbia University, New York, New York 10027, USA. [2]Department of Materials Science and Engineering, Yonsei University, Seoul 120-749, Republic of Korea. [3]School of Applied and Engineering Physics, Cornell University, Ithaca, New York 14853, USA. [4]KU-KIST Graduate School of Converging Science and Technology, Korea University, Seoul 136-701, Republic of Korea. [5]Department of Material Science and Engineering, Columbia University, New York, New York 10027, USA. [6]Center for Nanostructured Graphene (CNG), DTU Nanotech, Technical University of Denmark, Ørsteds Plads, 345E, Kgs. Lyngby 2800, Denmark. [7]National Institute for Materials Science, 1-1 Namiki, Tsukuba 305-0044, Japan. [8]Kavli Institute at Cornell for Nanoscale Science, Ithaca, New York 14853, USA. [9]Department of Electrical & Computer Engineering, University of Minnesota, Minneapolis, Minnesota 55455, USA. [10]Department of Physics, Harvard University, Cambridge, Massachusetts 02138, USA; [†]These authors contributed equally to this work. *e-mail: gwanlee@yonsei.ac.kr; jh2228@columbia.edu
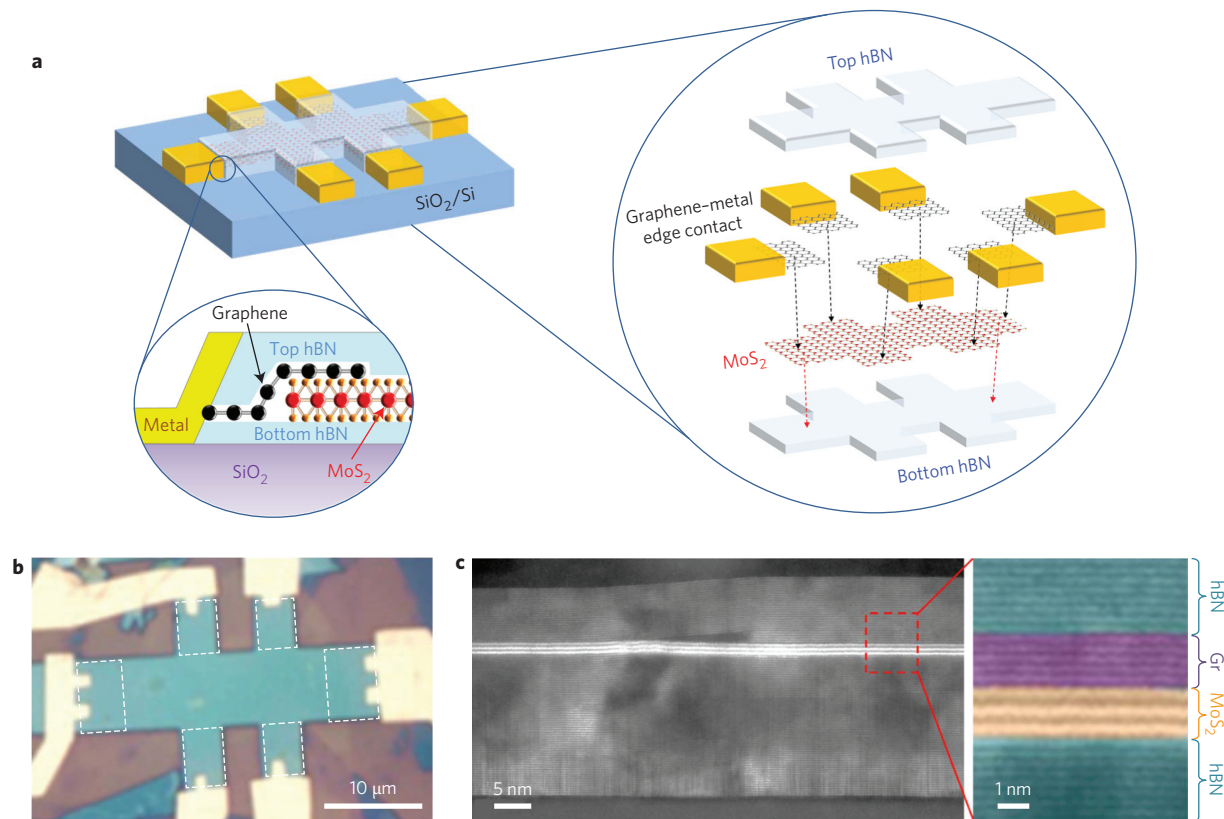
Figure 1 | vdW device structure and interface characterization. a, Schematic of the hBN-encapsulated MoS_2 multi-terminal device. The exploded view shows the individual components that constitute the heterostructure stack. Bottom: Zoom-in cross-sectional schematic of the metal–graphene–MoS_2 contact region. **b**, Optical microscope image of a fabricated device. Graphene contact regions are outlined by dashed lines. **c**, Cross-sectional STEM image of the fabricated device. The zoom-in false-colour image clearly shows the ultra-sharp interfaces between different layers (graphene, 5L; MoS_2, 3L; top hBN, 8 nm; bottom hBN, 19 nm).

transport behaviour that is near the ideal acoustic phonon limit at room temperature and ballistic over more than 15 μm at low T (ref. 34). These results were realized using a novel technique to create one-dimensional edge contacts to graphene exposed by plasma-etching an hBN/graphene/hBN stack. Such an approach has not yet proved effective with MoS_2. However, recent reports that graphene can create a high-quality electrical contact with MoS_2[18,35] motivated a hybrid scheme, in which the channel MoS_2 and multiple graphene 'leads' are encapsulated in hBN and the stack is etched to form graphene–metal edge contacts. This new scheme is distinct from previous approaches in that the entire MoS_2 channel is fully encapsulated and protected by hBN and we achieve multi-terminal graphene contacts without any contamination from the device fabrication process.

Figure 1a,b presents a schematic diagram and optical micrograph of a Hall bar device structure. A PDMS (polydimethylsiloxane) transfer technique[2] was used to place few-layer graphene flakes around the perimeter of a MoS_2 flake. These were then encapsulated between thicker hBN layers and the entire stack placed on a Si/SiO$_2$ wafer (Supplementary Fig. 1a). The stack was then shaped into a Hall bar geometry such that the hBN-encapsulated MoS_2 formed the channel. In the contact regions, the graphene overlaps the MoS_2 and extends to the edge, where it is in turn contacted by metal electrodes[34]. Details of the fabrication process are described in the Methods and Supplementary Section 1. High-resolution scanning transmission electron microscopy (STEM) (Fig. 1c; see also Supplementary Fig. 1b for a larger clean interface area of >3 μm) confirmed that the stacking method can produce ultraclean interfaces free of the residue that can be seen when an organic polymer film is used for stacking[36]. We note that although ohmic

contacts have also been achieved with metal–MoS_2 contacts through the deposition of small-workfunction metals, vacuum annealing and electrostatic gating[4,17,18], top-deposited metal electrodes are not compatible with hBN encapsulation.

For this study, a series of samples with thicknesses ranging from 1 to 6 layers (1–6L) were fabricated and measured. The number of layers was identified by Raman and photoluminescence analysis (Supplementary Section 2). All samples were obtained by mechanical exfoliation except for the 1L sample, for which we used chemical vapour deposition (CVD) grown monolayer MoS_2 because of the limited size of the mechanically exfoliated monolayers. The CVD-grown MoS_2 single crystal has been shown to exhibit high quality (from structural, electrical and optical measurements[37]), although the process of transferring it from the growth substrate may introduce more contamination than is the case with mechanically exfoliated flakes.

For each sample we performed temperature-dependent two-probe measurements to examine the quality of the graphene contacts. Figure 2a presents output curves (I_{ds}–V_{ds}) for a 4L MoS_2 device with a backgate voltage of $V_{bg} = 80$ V. The response is linear at room temperature and remains linear to low T, indicating an ohmic contact. Similar behaviour is seen for $V_{bg} > 20$ V, whereas gapped behaviour corresponding to non-ohmic contact is seen for $V_{bg} < 20$ V. This is consistent with previous studies that show a gate-tunable contact barrier between graphene and MoS_2 (refs 18,35). In addition, this establishes the gate voltage range over which multi-terminal measurements can be reliably performed. Figure 2b shows the measured four-terminal resistivity ρ (log scale) of the same sample with $V_{bg} = 20$ V to 80 V (corresponding to carrier densities of ~4.8×10^{12} to ~6.9×10^{12} cm^{-2}, respectively) and from room
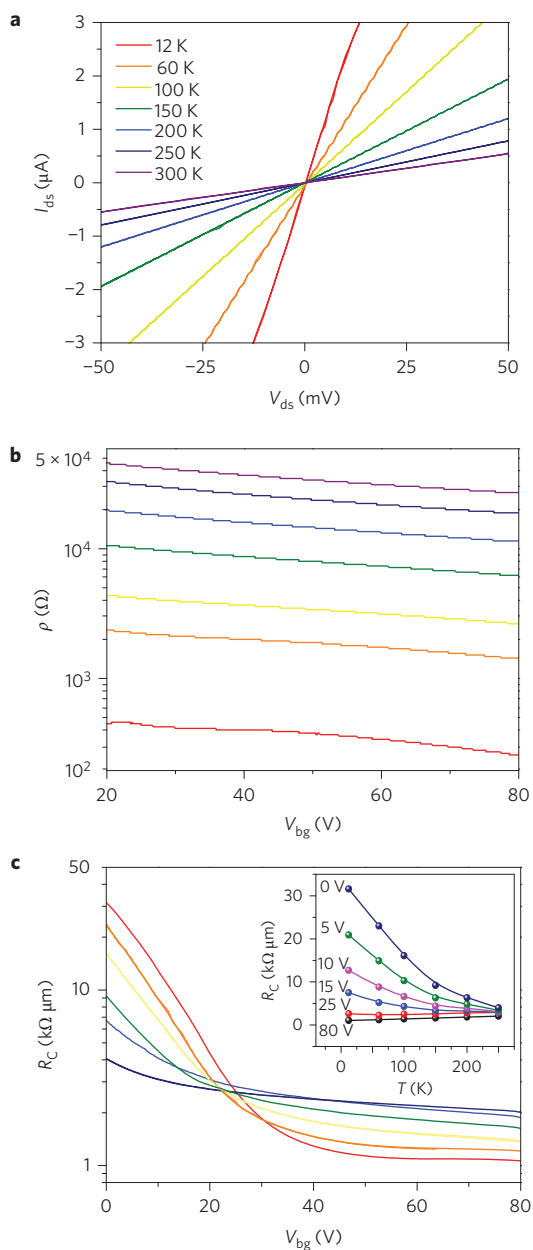
Figure 2 | Gate-tunable and temperature-dependent graphene–MoS$_2$ contacts. a, Output curves (I_{ds}–V_{ds}) of the hBN-encapsulated 4L MoS$_2$ device with graphene electrodes at different temperatures. Backgate voltage V_{bg} was maintained at 80 V with a carrier density of 6.85×10^{12} cm^{-2} in MoS$_2$. The linearity of the output curves confirms that the graphene–MoS$_2$ contact is ohmic at all temperatures. **b**, Resistivity ρ of 4L MoS$_2$ (log scale) as a function of V_{bg} at different temperatures. The resistivity decreases on cooling, showing metallic behaviour, reaching ~130 Ω at 12 K. The colour legend is the same as in **a** (from 300 K to 12 K). **c**, Contact resistance R_C of the same device (log scale) as a function of V_{bg} at different temperatures. The colour legend is the same as in **a** (but from 250 K to 12 K). Inset: R_C as a function of temperature at different V_{bg}. At high V_{bg} the contact resistance decreases when decreasing the temperature.

temperature to 12 K. ρ decreases with increasing V_{bg}, as expected for an n-type semiconductor. With decreasing temperature, ρ drops dramatically over the entire accessible range of V_{bg}, reaching 130 Ω at 12 K. All of the samples studied exhibited similar behaviour: n-type semiconducting behaviour and metallic temperature dependence in the gate voltage accessible to four-terminal measurements.

By comparing the two- and four-terminal results, the contact resistance can be determined (Supplementary Section 3). The results for the 4L MoS$_2$ device, as shown in Fig. 2c, directly demonstrate that the contact resistance can be tuned by the backgate voltage. In fact, a small contact resistance of ~2 kΩ μm can be reliably achieved at a large gate voltage at room temperature. This probably reflects primarily the graphene–MoS$_2$ junction resistance, as both the graphene resistance and the graphene–metal contact resistance should be substantially less[34]. Below $V_{bg} = 20$ V, the contact resistance increases on cooling, indicating activated transport across a contact barrier. However, above $V_{bg} = 20$ V, the contact resistance decreases upon cooling, reaching a low-T value of ~1 kΩ μm above $V_{bg} = 50$ V. This metallic behaviour directly demonstrates that low-resistance contacts, with no thermal activation, can be achieved at sufficiently high gate voltage. Similar behaviour was observed in all samples (Supplementary Fig. 3), with contact resistance at high V_{bg} ranging from ~2 to 20 kΩ μm at room temperature and from ~0.7 to 10 kΩ μm at low T. These values are comparable to the room-temperature values reported previously for graphene[38] and metal[39–41] contacts, but larger than the best contacts achieved by MoS$_2$ phase engineering (0.2–0.3 kΩ μm)[29]. Owing to the increase in bandgap with decreasing thickness, the value of V_{bg} required to achieve ohmic contact is larger for thinner samples.

Scattering mechanism in MoS$_2$

To examine the quality of the hBN-encapsulated devices and determine the scattering mechanisms limiting the carrier mobility of MoS$_2$, the Hall mobility $\mu_{Hall}(T)$ was derived from $\rho(T)$ and the carrier density $n(V_{bg})$ (obtained by Hall effect measurements, Supplementary Section 4). Figure 3a shows μ_{Hall} for the 1–6L samples as a function of temperature, at carrier densities ranging from 4.0×10^{12} to 1.2×10^{13} cm^{-2} (Fig. 3b and Supplementary Table 1). Thinner samples were measured at the higher carrier densities required to achieve ohmic contact. For all samples, mobility increases with decreasing temperature and saturates at a constant value at low T. The low-T mobility in our devices is much higher than previously reported values and there is no sign of a metal–insulator transition as observed at similar carrier densities around 1×10^{13} cm^{-2} in SiO$_2$-supported MoS$_2$ (refs 8,9,30,32,33). This strongly suggests that extrinsic scattering and disorder (either from SiO$_2$ or from processing with polymer resists) has been the primary source of the non-metallic behaviour in MoS$_2$ measured to date.

The measured mobility curves can be reasonably fitted to a simple functional form: $1/\mu(T) = 1/\mu_{imp} + 1/\mu_{ph}(T)$, where μ_{imp} is the contribution from impurity scattering and μ_{ph} is the temperature-dependent contribution due to phonon scattering. In all samples, the fitted $\mu_{ph}(T)$ is well described by a power law ($\mu_{ph} \sim T^{-\gamma}$) above 100 K (Supplementary Fig. 7). This behaviour is consistent with mobility limited by MoS$_2$ optical phonons, which is theoretically predicted to have an exponent of ~1.69 in monolayer[23] and ~2.5 in bulk[42] MoS$_2$ at $T > 100$ K. Although this power-law behaviour has been observed in experiments conducted by other groups[8,9,30], a stronger temperature dependence was observed in our devices, with the exponent γ ranging from 1.9 to 2.5 (inset table in Fig. 3a), as opposed to 0.55–1.7 as reported previously[8,9]. We also note that the room-temperature mobility, which is dominated by phonon scattering in all the samples, is seen to vary from 40 to 120 cm^2 V^{-1} s^{-1}. At this point we can find no satisfactory explanation for this variation: there is no discernible trend with thickness and no variation in the gamma value with carrier density (Supplementary Fig. 8). Finally, we note that a deviation from the simple form $\mu_{ph} \sim T^{-\gamma}$ in high-mobility samples below 100 K may indicate acoustic phonon scattering, although further study is needed to fully explore this regime.
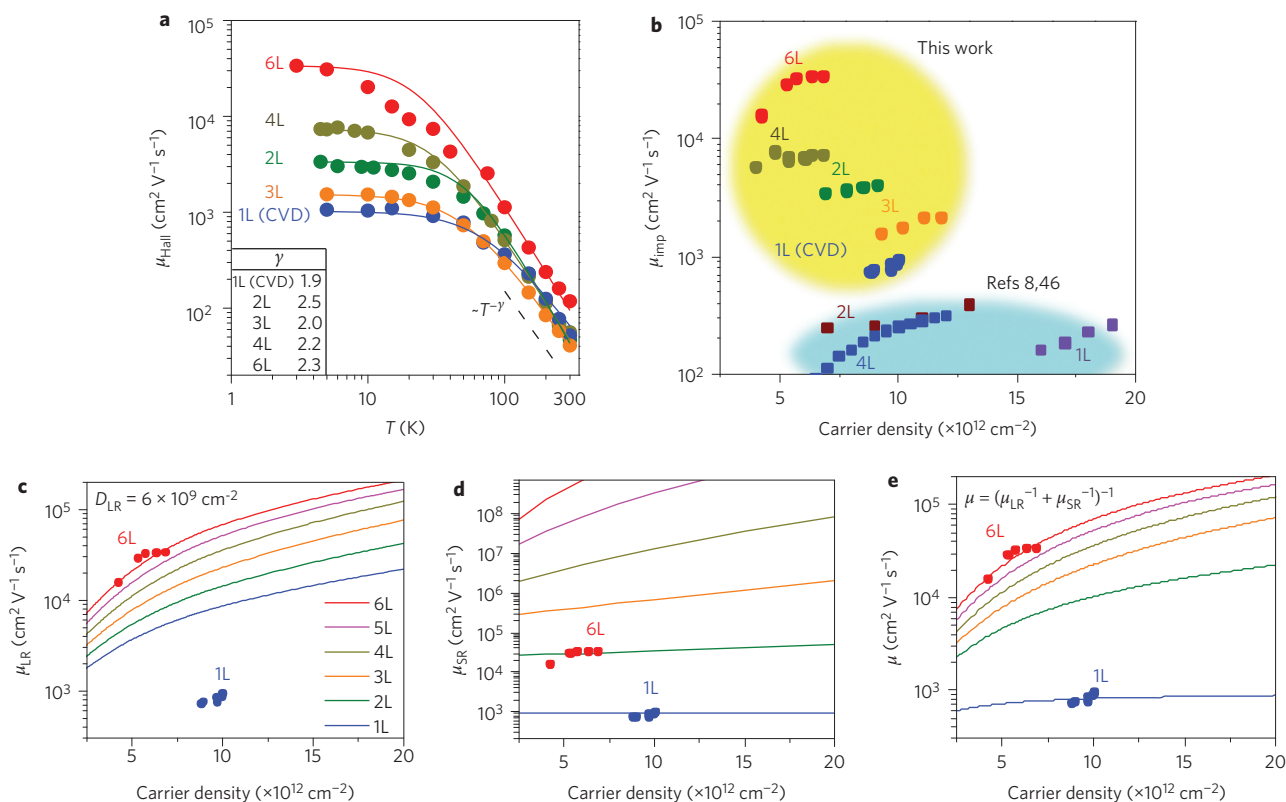
Figure 3 | Temperature, carrier density dependence of Hall mobility and scattering mechanism. a, Hall mobility of hBN-encapsulated MoS_2 devices (with different numbers of layers of MoS_2) as a function of temperature. To maintain ohmic contact, a finite V_{bg} was applied. The measured carrier densities obtained from Hall measurements for each device are listed in Supplementary Table 1. The solid fitting lines are drawn by the model described in the main text. All fitting parameters are listed in Supplementary Table 1. As a visual guide, the dashed line shows the power law $\mu_{ph} \sim T^{-\gamma}$, and fitted values of γ for each device are listed in the inset table. **b**, Impurity-limited mobility (μ_{imp}) as a function of the MoS_2 carrier density. For comparison, previously reported values from MoS_2 on SiO_2 substrates (refs 8,46) are plotted. **c–e**, The solid lines show the theoretically calculated long-range (LR) impurity-limited mobility (**c**), short-range (SR) impurity-limited mobility (**d**) and mobility including both LR and SR based on Matthiessen's rule, $1/\mu = 1/\mu_{LR} + 1/\mu_{SR}$, as a function of carrier density for 1L to 6L MoS_2 (**e**). Experimental data from 1L and 6L MoS_2 are shown as circles (**c–e**).

At the lowest temperature, phonon scattering is suppressed and the residual resistivity is due to dominant long-range Coulomb impurities or short-range atomic defects[43–45], captured in the measured quantity μ_{imp}. Figure 3b shows the derived values of μ_{imp} as a function of carrier density n. For each sample, μ_{imp} increases with n, with maximum values ranging from $1{,}020$ cm^2 V^{-1} s^{-1} in the CVD monolayer to $34{,}000$ cm^2 V^{-1} s^{-1} for 6L MoS_2, up to two orders of magnitude higher than previously reported values[8,46] (Fig. 3b and Supplementary Table 1). These basic trends allow us to rule out scattering due to impurities or defects located within the MoS_2 itself: bulk charged impurities should give rise to thickness-independent mobility, and short-range scatterers due to atomic defects should give rise to a density-independent mobility[45]. On the other hand, interfacial scatterers, including both Coulomb impurities and short-range defects, which are limiting scattering mechanisms in high-quality conventional two-dimensional electron gas systems (2DEGs)[44], are promising candidates. Indeed, PDMS transfer, while substantially cleaner than methods involving organic polymers, can potentially introduce adsorbates to the top MoS_2 surface.

To understand the effects of interfacial scattering on samples of different thickness, we modelled interfacial Coulomb and short-range scattering as a function of carrier density, for samples from 1L to 6L in thickness. For Coulomb scattering we used a model based on a perturbative approach by Stern[47], from which we obtained the screened Coulomb potential used in the mobility calculation. This model has also been commonly used in the context of semiconductor devices (Supplementary Section 8). Within the model, increasing carrier density enhances screening of the interfacial Coulomb potential, which leads to improved carrier mobility, and increasing the thickness of MoS_2 redistributes the charge centroid further from the interface, also resulting in enhancement of mobility. The calculated mobility is shown in Fig. 3c, assuming the same impurity concentration of 6×10^9 cm^{-2} (chosen to match the 6L data) located at the top MoS_2 interface, for devices with different numbers of layers. Although the qualitative trend of increasing mobility with layer number and carrier density is consistent with the model, the model fails to account for the observed large thickness dependence of more than an order of magnitude between the 1L and 6L devices. Changes in the model calculations, including the effects of band structure change with increasing layer thickness, are discussed in Supplementary Section 8.

We next consider interfacial short-range scatterers with atomically localized scattering potentials, which can be modelled as delta-function potentials within the same framework as used above. Quantum lifetime measurements, as discussed later in this Article, suggest that these scatterers strongly dominate electronic transport in the 1L devices. We therefore set the interfacial short-range scattering parameter (the product of scattering potential and defect density, Supplementary Section 8) to fit the mobility of the 1L device. In this case, for the same interfacial scattering the mobility increases rapidly with sample thickness—much more than is observed experimentally.
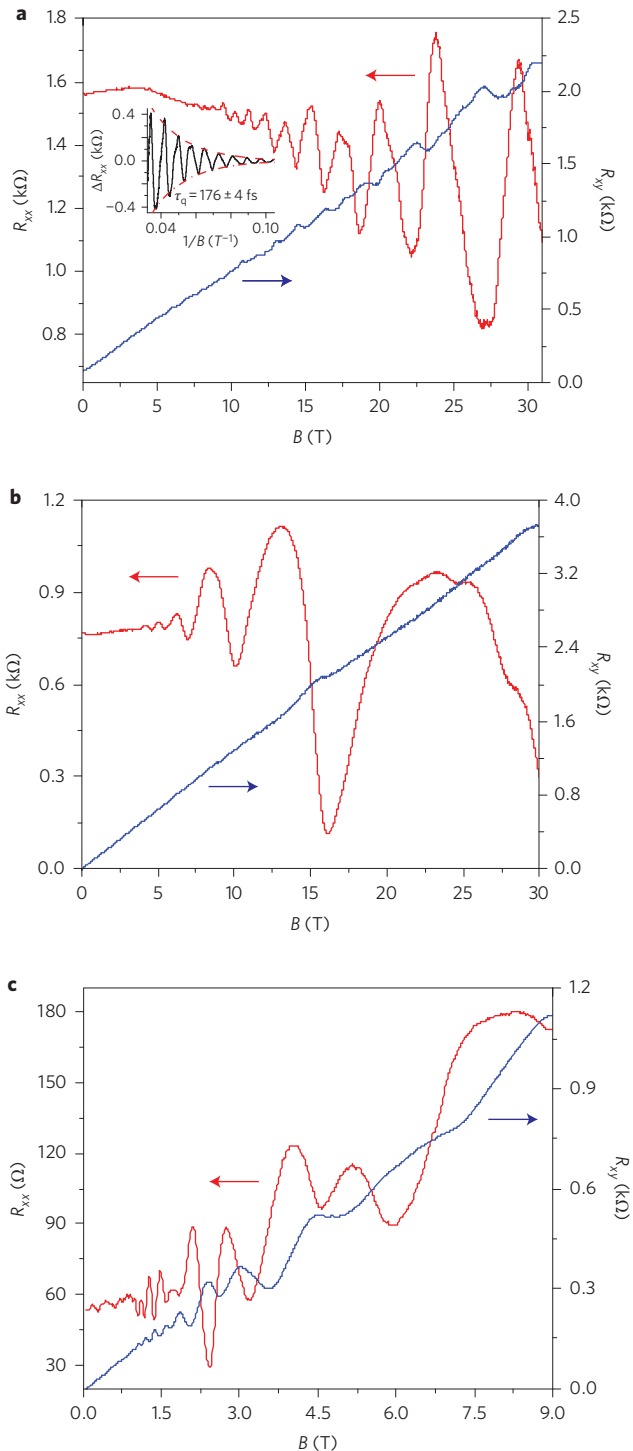
Figure 4 | Observation of Shubnikov–de Haas oscillations in an hBN-encapsulated MoS$_2$ device. a, Longitudinal resistance R_{xx} (red curve) and Hall resistance R_{xy} (blue curve) of an hBN-encapsulated CVD 1L MoS$_2$ device as a function of magnetic field B measured at 0.3 K and with a carrier density of 9.7×10^{12} cm^{-2}. Inset: Oscillation amplitude (black curve) as a function of $1/B$ after subtraction of the magnetoresistance background. The quantum scattering time extracted from the fitted Dingle plot (red dashed line) is 176 fs. **b**, R_{xx} (red curve) and R_{xy} (blue curve) of the hBN-encapsulated 4L MoS$_2$ device as a function of B. Hall measurements were conducted at 0.3 K and at a carrier density of 4.9×10^{12} cm^{-2}. **c**, R_{xx} (red curve) and R_{xy} (blue curve) of an hBN-encapsulated 6L MoS$_2$ device as a function of B. Hall measurements were conducted at 3 K and with a carrier density of 5.3×10^{12} cm^{-2}.

Based on this analysis, we propose that the interfaces in our devices introduce both long-range Coulomb scattering and short-range scattering. In this case, we can calculate the total extrinsic mobility using Matthiessen's rule. The combination of long- and short-range scatterers provides better agreement with the observed layer-dependent mobility, as shown in Fig. 3e, a salient point that we will revisit again later in a quantum oscillations study. Of course, a perfect match to experiment is not expected due to sample-to-sample variations in impurity density. We also note that the long-range impurity density of 6×10^9 cm^{-2} is two orders of magnitude smaller than is typically obtained for graphene on SiO$_2$, and hence accounts for the two orders of magnitude larger mobility we obtained as compared to the best reported devices[8,46].

Observation of Shubnikov–de Haas oscillations in MoS$_2$

Figure 4 presents the longitudinal (R_{xx}) and Hall (R_{xy}) resistance of the monolayer (Fig. 4a), 4L (Fig. 4b) and 6L (Fig. 4c) MoS$_2$ samples as a function of applied magnetic field. We observe pronounced Shubnikov–de Haas (SdH) oscillations in MoS$_2$, providing additional strong evidence of high quality and homogeneity in the heterostructure devices. In the highest-mobility (6L) sample (Fig. 4c), the onset of SdH oscillations is close to 1 T, further confirming its ultra-high mobility. Encouragingly, the high-field Hall resistance (blue curve, R_{xy}) begins to reveal plateau-like structures at high magnetic fields coinciding with R_{xx} minima. These emerging features were similarly observed in early studies of graphene samples with moderate mobility[48], giving hope that fully developed quantum Hall states can be observed with further improvements in sample quality. The periodicity of the SdH oscillations can be used to estimate the carrier density, or equivalently to measure the level degeneracy g for a known density (for details see Supplementary Section 7). For the 1L samples we observe $2 < g < 4$, indicating that the bands may be partially valley–spin split (the multi-band nature of the 6L sample complicates this analysis). This is consistent with the extra SdH oscillations that begin to emerge at high fields, but more detailed study is required to explore this splitting in detail.

The quantum scattering time τ_q, which is limited by both small- and large-angle scattering (which destroys quantized cyclotron orbits), can be estimated from the magnetic field corresponding to the onset of SdH oscillations, following the relation $\mu_q = e\tau_q/m^* \approx 1/B_q$ (ref. 49), where e is the electron charge and m^* is the effective mass obtained from *ab initio* band structure calculations[50]. This yields quantum mobilities for 1L, 4L and 6L MoS$_2$ of ~1,400, ~3,100 and ~10,000 cm^2 V^{-1} s^{-1}, respectively. A more accurate estimate of τ_q in MoS$_2$ can be obtained using a Dingle plot (Supplementary Fig. 9), a well-established method in conventional 2DEGs (for details see Supplementary Section 6). The inset of Fig. 4a shows the SdH oscillations of 1L MoS$_2$ after subtraction of a magnetoresistance background, as function of $1/B$. The red dashed line is the fitted envelope, from which we estimate a quantum scattering time of $\tau_q = 176$ fs. We show the values of τ_q obtained using both methods (oscillation onset and Dingle plots) in Supplementary Fig. 9c. The ratio of transport to quantum scattering time can provide additional evidence of the dominant scattering sources. In our samples, a ratio near 1 in 1L devices indicates predominantly short-range scattering, and an increase in τ_t/τ_q with increasing thickness indicates a crossover to long-range scattering. This trend is consistent with our previous physical picture of low-T electronic transport dominated by a mix of short- and long-range interfacial impurities.

Conclusion

We have demonstrated a van der Waals heterostructure device platform in which an atomically thin MoS$_2$ layer is encapsulated by hBN and contacted by graphene. The van der Waals heterostructure provides a standard device platform that enables us to measure the

intrinsic electrical transport of two-dimensional materials and achieve high-mobility two-dimensional devices in which to study their unique transport properties and novel quantum physics. By forming robust and tunable electrical contacts and dramatically reducing the interfacial impurities, intrinsic electron–phonon scattering can be observed at high T, and substantially improved mobility can be achieved at low T. This has enabled the first observation of SdH oscillations in MoS_2. Modelling and quantum lifetime analysis suggest that a combination of short- and long-range interfacial scattering limits the low-T mobility, indicating that further improvements should be possible.

Methods

Device fabrication. The $hBN/MoS_2/graphene/hBN$ stacks were fabricated using the 'PDMS transfer'[2] technique on 285 nm SiO_2/Si substrates. The transfer techniques are described in detail in Supplementary Section 1. The stacks were then shaped to the desired Hall bar structure through electron-beam patterning and reactive ion etching (RIE) with a mixture of CHF_3 and O_2. Finally, metal leads were patterned by electron-beam lithography and subsequent deposition of metals (Cr 1 nm/Pd 20 nm/Au 50 nm). The metal leads make edge-contact to the graphene electrodes, as reported previously[34].

TEM sample preparation. For high-resolution imaging we fabricated a cross-sectional TEM lift-out sample from the finished encapsulated devices, using an FEI Strata 400 dual-beam focused ion beam device. STEM imaging was carried out with an FEI Tecnai F-20 STEM operated at 200 kV, with a 9.6 mrad convergence semi-angle and high-angle annular dark-field detector. False colouring was added by hand.

Electrical measurements and magneto-transport measurements. Two-terminal transport characteristics were measured by applying a d.c. bias (Keithley 2400) to the source and gate electrodes and measuring the drain current using a current amplifier (DL 1211). For four-terminal measurements, a standard lock-in amplifier (SR830) was used to measure the voltage drop across the channel with constant current bias. Magneto-transport measurements were performed in a Physical Property Measurement System (PPMS; Fig. 4c) and a He_3 cryostat at the National High Magnetic Field Laboratory (NHMFL) (Fig. 4a,b).

References

1. Radisavljevic, B., Radenovic, A., Brivio, J., Giacometti, V. & Kis, A. Single-layer MoS₂ transistors. *Nature Nanotech.* **6,** 147–150 (2011).
2. Lee, G. H. *et al.* Flexible and transparent MoS₂ field-effect transistors on hexagonal boron nitride–graphene heterostructures. *ACS Nano* **7,** 7931–7936 (2013).
3. Mak, K., Lee, C., Hone, J., Shan, J. & Heinz, T. Atomically thin MoS₂: a new direct-gap semiconductor. *Phys. Rev. Lett.* **105,** 136805 (2010).
4. Lee, C. H. *et al.* Atomically thin p–n junctions with van der Waals heterointerfaces. *Nature Nanotech.* **9,** 676–681 (2014).
5. Lee, C. *et al.* Anomalous lattice vibrations of single- and few-layer MoS₂. *ACS Nano* **4,** 2695–2700 (2010).
6. Kim, S. *et al.* High-mobility and low-power thin-film transistors based on multilayer MoS₂ crystals. *Nature Commun.* **3,** 1011 (2012).
7. Das, S., Chen, H-Y., Penumatcha, A. & Appenzeller, J. High performance multilayer MoS₂ with scandium contacts. *Nano Lett.* **13,** 100–105 (2013).
8. Baugher, B., Churchill, H., Yang, Y. & Jarillo-Herrero, P. Intrinsic electronic transport properties of high-quality monolayer and bilayer MoS₂. *Nano Lett.* **13,** 4212–4216 (2013).
9. Radisavljevic, B. & Kis, A. Mobility engineering and a metal–insulator transition in monolayer MoS₂. *Nature Mater.* **12,** 815–820 (2013).
10. Xiao, D., Liu, G-B., Feng, W., Xu, X. & Yao, W. Coupled spin and valley physics in monolayers of MoS₂ and other group-VI dichalcogenides. *Phys. Rev. Lett.* **108,** 196802 (2012).
11. Mak, K., McGill, K., Park, J. & McEuen, P. Valleytronics. The valley Hall effect in MoS₂ transistors. *Science* **344,** 1489–1492 (2014).
12. Zeng, H., Dai, J., Yao, W., Xiao, D. & Cui, X. Valley polarization in MoS₂ monolayers by optical pumping. *Nature Nanotech.* **7,** 490–493 (2012).
13. Jiang, T. *et al.* Valley and band structure engineering of folded MoS₂ bilayers. *Nature Nanotech.* **9,** 825–829 (2014).
14. Mak, K., He, K., Shan, J. & Heinz, T. Control of valley polarization in monolayer MoS₂ by optical helicity. *Nature Nanotech.* **7,** 494–498 (2012).
15. Bao, W., Cai, X., Kim, D., Sridhara, K. & Fuhrer, M. High mobility ambipolar MoS₂ field-effect transistors: substrate and dielectric effects. *Appl. Phys. Lett.* **102,** 042104 (2013).
16. Choi, M., Lee, G. H., Yu, Y., Lee, D. & Lee, S. Controlled charge trapping by molybdenum disulphide and graphene in ultrathin heterostructured memory devices. *Nature Commun.* **4,** 1642 (2013).
17. Wang, H. *et al.* Integrated circuits based on bilayer MoS₂ transistors. *Nano Lett.* **12,** 4674–4680 (2012).
18. Yu, L. *et al.* Graphene/MoS₂ hybrid technology for large-scale two-dimensional electronics. *Nano Lett.* **14,** 3055–3063 (2014).
19. Sundaram, R., Engel, M., Lombardo, A. & Krupke, R. Electroluminescence in single layer MoS₂. *Nano Lett.* **13,** 1416–1421 (2013).
20. Britnell, L. *et al.* Strong light–matter interactions in heterostructures of atomically thin films. *Science* **340,** 1311–1314 (2013).
21. Yoon, J. *et al.* Highly flexible and transparent multilayer MoS₂ transistors with graphene electrodes. *Small* **9,** 3295–3300 (2013).
22. Qiu, H. *et al.* Electrical characterization of back-gated bi-layer MoS₂ field-effect transistors and the effect of ambient on their performances. *Appl. Phys. Lett.* **100,** 123104 (2012).
23. Kaasbjerg, K., Thygesen, K. & Jacobsen, K. Phonon-limited mobility in n-type single-layer MoS₂ from first principles. *Phys. Rev. B* **85,** 115317 (2012).
24. Ma, N. & Jena, D. Charge scattering and mobility in atomically thin semiconductors. *Phys. Rev. X* **4,** 011043 (2014).
25. Li, X. *et al.* Intrinsic electrical transport properties of monolayer silicene and MoS₂ from first principles. *Phys. Rev. B* **87,** 115418 (2013).
26. Novoselov, K. *et al.* Two-dimensional atomic crystals. *Proc. Natl Acad. Sci. USA* **102,** 10451–10453 (2005).
27. Kappera, R., Voiry, D., Yalcin, S. E., Jen, W. & Acerce, M. Metallic 1T phase source/drain electrodes for field effect transistors from chemical vapor deposited MoS₂. *Appl. Phys. Lett.* **2,** 092516 (2014).
28. Guo, Y. *et al.* Study on the resistance distribution at the contact between molybdenum disulfide and metals. *ACS Nano* **8,** 7771–7779 (2014).
29. Kappera, R. *et al.* Phase-engineered low-resistance contacts for ultrathin MoS₂ transistors. *Nature Mater.* **13,** 1128–1134 (2014).
30. Schmidt, H. *et al.* Transport properties of monolayer MoS₂ grown by chemical vapor deposition. *Nano Lett.* **14,** 1909–1913 (2014).
31. Yu, Z. *et al.* Towards intrinsic charge transport in monolayer molybdenum disulfide by defect and interface engineering. *Nature Commun.* **5,** 5290 (2014).
32. Zhu, W. *et al.* Electronic transport and device prospects of monolayer molybdenum disulphide grown by chemical vapour deposition. *Nature Commun.* **5,** 3078 (2014).
33. Qiu, H. *et al.* Hopping transport through defect-induced localized states in molybdenum disulphide. *Nature Commun.* **4,** 2642 (2013).
34. Wang, L. *et al.* One-dimensional electrical contact to a two-dimensional material. *Science* **342,** 614–617 (2013).
35. Roy, T. *et al.* Field-effect transistors built from all two-dimensional material components. *ACS Nano* **8,** 6256–6264 (2014).
36. Haigh, S., Gholinia, A., Jalil, R., Romani, S. & Britnell, L. Cross-sectional imaging of individual layers and buried interfaces of graphene-based heterostructures and superlattices. *Nature Mater.* **11,** 764–767 (2012).
37. Van der Zande, A. M. *et al.* Grains and grain boundaries in highly crystalline monolayer molybdenum disulphide. *Nature Mater.* **12,** 554–561 (2013).
38. Du, Y., Yang, L., Liu, H. & Ye, P. Contact research strategy for emerging molybdenum disulfide and other two-dimensional field-effect transistors. *APL Mater.* **2,** 092510 (2014).
39. Das, S. & Appenzeller, J. Where does the current flow in two-dimensional layered systems? *Nano Lett.* **13,** 3396–3402 (2013).
40. Liu, H., Neal, A. T. & Ye, P. D. Channel length scaling of MoS₂ MOSFETs. *ACS Nano* **6,** 8563–8569 (2012).
41. Liu, H. *et al.* Switching mechanism in single-layer molybdenum disulfide transistors: an insight into current flow across Schottky barriers. *ACS Nano* **8,** 1031–1038 (2013).
42. Fivaz, R. & Mooser, E. Mobility of charge carriers in semiconducting layer structures. *Phys. Rev.* **163,** 743755 (1967).
43. Chen, J-H., Jang, C., Xiao, S., Ishigami, M. & Fuhrer, M. S. Intrinsic and extrinsic performance limits of graphene devices on SiO₂. *Nature Nanotech.* **3,** 206–209 (2008).
44. Ando, T., Fowler, A. B. & Stern, F. Electronic properties of two-dimensional systems. *Rev. Mod. Phys.* **54,** 437–672 (1982).
45. Sarma, D., Adam, S., Hwang, E. & Rossi, E. Electronic transport in two-dimensional graphene. *Rev. Mod. Phys.* **83,** 407–470 (2011).
46. Neal, A., Liu, H., Gu, J. & Ye, P. Magneto-transport in MoS₂: phase coherence, spin–orbit scattering, and the hall factor. *ACS Nano* **7,** 7077–1082 (2013).
47. Stern, F. & Howad, W. E. Properties of semiconductor surface inversion layers in the electric quantum limit. *Phys. Rev.* **163,** 816–835 (1967).
48. Novoselov, K. *et al.* Electric field effect in atomically thin carbon films. *Science* **306,** 666–669 (2004).
49. Kretinin, A. V. *et al.* Electronic properties of graphene encapsulated with different two-dimensional atomic crystals. *Nano Lett.* **14,** 3270–3276 (2014).
50. Liu, G-B., Shan, W-Y., Yao, Y., Yao, W. & Xiao, D. Three-band tight-binding model for monolayers of group-VIB transition metal dichalcogenides. *Phys. Rev. B* **88,** 085433 (2013).

Author contributions

X.C. and G-H.L. designed the research project and supervised the experiment. X.C., G-H.L., Y.D.K., G.A., C-H.L., F.Y., F.P., B.S.J. and L.W. fabricated the devices. X.C., G-H.L. and Y.D.K. performed device measurements with supervision from P.K. and J.H. X.C., G-H.L., G.A. and X.Z. performed optical spectroscopy and data analysis. D.A.C. grew and prepared the CVD MoS_2 sample. T.L. performed theoretical calculations. K.W. and T.T. prepared hBN samples. P.Y.H. and D.A.M. performed TEM analyses. X.C., G-H.L., Y.D.K. and J.H. analysed the data and wrote the manuscript.

Additional information

Supplementary information is available in the online version of the paper. Reprints and permissions information is available online at www.nature.com/reprints. Correspondence and requests for materials should be addressed to G.H.L. and J.H.

Competing financial interests

The authors declare no competing financial interests.